AGU PUBLICATIONS

Geophysical Research Letters

RESEARCH LETTER
10.1002/2016GL071140

Key Points:
- Tuffites and marine sediments are characterized by Q_P values less than 40
- High-Q_P anomalies may be explained as consolidated volcanic materials or fluid effects
- A fluid-filled densely fractured rock volume has been imaged as the rim of caldera

Supporting Information:
- Supporting Information S1

Correspondence to:
V. Serlenga,
vincenzo.serlenga@unina.it

Citation:
Serlenga, V., S. de Lorenzo, G. Russo, O. Amoroso, S. Garambois, J. Virieux, and A. Zollo (2016), A three-dimensional Q_P imaging of the shallowest subsurface of Campi Flegrei offshore caldera, southern Italy, *Geophys. Res. Lett.*, *43*, 11,209–11,218, doi:10.1002/2016GL071140.

Received 7 SEP 2016
Accepted 26 OCT 2016
Accepted article online 28 OCT 2016
Published online 12 NOV 2016

A three-dimensional Q_P imaging of the shallowest subsurface of Campi Flegrei offshore caldera, southern Italy

Vincenzo Serlenga[1,2], Salvatore de Lorenzo[3], Guido Russo[1], Ortensia Amoroso[2], Stephane Garambois[4], Jean Virieux[4], and Aldo Zollo[1]

[1]Dipartimento di Fisica "Ettore Pancini", University of Napoli Federico II, Naples, Italy, [2]Amra SCARL, Naples, Italy, [3]Dipartimento di Scienze della Terra e Geoambientali, Università di Bari "Aldo Moro", Bari, Italy, [4]ISTerre, Université Grenoble Alpes, CNRS, Grenoble, France

Abstract To improve the knowledge of the shallowest subsurface of Campi Flegrei caldera, a 3-D *P* wave attenuation tomography of the area was performed. We analyzed about 18,000 active seismic traces, which provided a data set of 11,873 Δt^* measurements, e.g., the differential travel times to quality factor ratios. These were inverted through an adapted tomographic inversion procedure. The 3-D tomographic images reveal an average Q_P about 70, interpreted as water-saturated volcanic and marine sediments. An arc-like, low-Q_P structure at 0.5–1 km depths was interpreted as a densely fractured, fluid-saturated rock volume, well matching the buried rim of Campi Flegrei caldera. The spatial distribution of high- and low-Q_P bodies in the inner caldera is correlated with low-V_p values and may reflect either the differences in the percentage of fluid saturation of sediments or the presence of vapor state fluids beneath fumarole manifestations.

1. Introduction

In the past, several tomographic studies were performed in volcanic areas to determine 3-D *P* and *S* wave velocity structures [e.g., *Benz et al.*, 1996; *Judenherc and Zollo*, 2004; *Rowlands et al.*, 2005; *Brenguier et al.*, 2006; *Sherburn et al.*, 2006; *Battaglia et al.*, 2008]. This geological context, however, is characterized by strong lateral contrasts, associated to unconsolidated volcanoclastic deposits, multifractured media, presence of fluids, melt, and aquifers. Then, the only knowledge of elastic properties may be not sufficient for a complete understanding of volcanic dynamics. Indeed, body wave quality factor *Q*, describing the anelasticity of the medium, is more sensitive than elastic parameters to physical properties like temperature, porosity, permeability, and level of rock saturation [*Sanders et al.*, 1995]. Therefore, for volcanic areas, it is very useful to associate 3-D attenuation tomography to common elastic imaging as highlighted by several studies performed throughout the world [*Prudencio et al.*, 2013; *De Siena et al.*, 2014; *Prudencio et al.*, 2015a; *Prudencio et al.*, 2015b; *Prudencio et al.*, 2015c].

The purpose of this work is to add information, derived from Q_P images, integrating the knowledge on Campi Flegrei (CF hereinafter) subsurface in terms of rock rheology and physical properties. The primary aim is to detail presence of fluids in the shallowest subsurface of offshore CF caldera.

CF is a resurgent caldera located 15 km west of Naples, southern Italy. Its present shape is greatly affected by two large explosive eruptions occurring 39 kyr and 15 kyr ago [*Deino et al.*, 2004; *De Vivo et al.*, 2001]. Two main bradyseismic crises were recorded in the last 50 years (1970–1972 and 1982–1984) consisting in ground deformations, which led to a cumulative uplift of 3.5 m in Pozzuoli town [*Orsi et al.*, 1999]. Recently, many geophysical studies were performed to characterize the deep system of CF caldera. Tomographic studies [*Zollo et al.*, 2003; *Judenherc and Zollo*, 2004; *Chiarabba and Moretti*, 2006; *Battaglia et al.*, 2008; *Dello Iacono et al.*, 2009] mainly imaged an annular positive V_p anomaly at about 0.6–2 km depths. It well matched positive density anomaly found by *Capuano and Achauer* [2003] and *Capuano et al.* [2013], and it was interpreted as the buried rim of CF caldera, composed of an intercalation of consolidated lavas and tuffs. *Vanorio et al.* [2005], *Chiarabba and Moretti* [2006], and *Dello Iacono et al.* [2009] also highlighted a high V_p/V_s ratio in the shallower part of caldera due to water-saturated volcanic deposits. Velocity studies provided an image of the whole caldera up to 5–6 km depth; otherwise, less information are available on the intrinsic attenuation structure of CF: *de Lorenzo et al.* [2001] and *De Siena et al.* [2010] focused mainly on the northern part of CF caldera retrieving both high-Q_P and low-Q_P anomalies. The correlation of these attenuation images with high

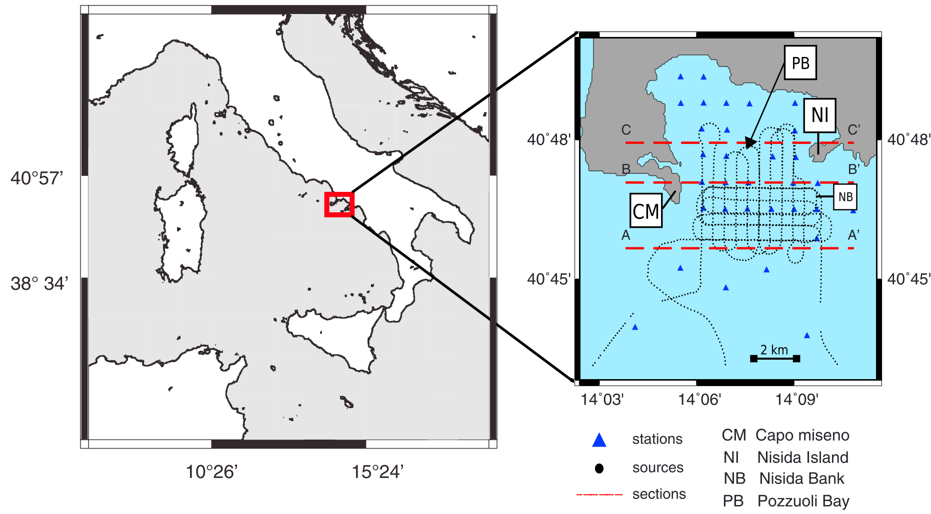

Figure 1. Geographical location of investigated area with respect to Italy. Blue triangles: seismic stations; black dots: positions of shots in Pozzuoli Bay; red dashed lines: traces of the tomographic sections shown in Figure 3.

temperature zones and *Vp* and *Vp/Vs* images permitted to identify thermal effects and hydrothermal basins otherwise ignored by simple V_p and V_s tomographic analyses.

In this study we use active seismic data to retrieve a 3-D Q_P tomography of CF. A refined procedure of differential t^* measurements (hereinafter Δt^*) is adopted through the spectral ratio method. Then, an adapted tomographic inversion technique is applied to retrieve the 3-D Q_P image of CF caldera. Final results are interpreted by correlating attenuation images with previous results from different geophysical imaging techniques.

2. Data and Methods

2.1. Data Analysis

The database used for this work was acquired during an active seismic campaign (SEismic Reflection/Refraction Acquisition Project for Imaging complex volcanic Structures (SERAPIS) experiment) performed in September 2001 in an area of 50×50 km^2 including the Bays of Naples and Pozzuoli (Figure 1).

The experiment consisted in 5000 shots recorded at a network of 72 ocean bottom receivers (OBSs) and 84 land seismographs. The OBSs were equipped with 4.5 Hz three-component sensors. Signals were recorded with a time sampling of 0.004 s. The original processing of SERAPIS data set provided more than 85,000 manually picked *P* wave first arrivals [*Judenherc and Zollo*, 2004; *Capuano et al.*, 2006]. Since we aim to study the anelastic properties of subsurface of Pozzuoli Bay, signals referring to shots and receivers in that subarea are selected. Therefore, we collected totally 41,768 *P* wave phase picks, available from previous analyses.

Following *Teng* [1968], the procedure of retrieving a three-dimensional Q_P image requires two steps: the Δt^* measurement and the spatial inversion of the selected Δt^* data set. First, the spectral ratio method [*Teng*, 1968] is applied to our data set. To take into account path effects on seismic signals, a refined procedure of the technique is applied. The displacement spectrum $A_{ij}(f)$ of the *i*th event observed at the *j*th station at distance *x* from the source is

$$A_{i,j}(f) = S_i(f)C_j(f)G(f,x)I(f)\exp\left(-\pi t^*{}_{i,j}f\right), \tag{1}$$

where the function $S_i(f)$ represents the source term and site effects are described by $C_j(f)$. The effects of Earth's velocity structure on seismic signals (elastic Green's function) are represented by $G(f, x)$; the instrumental response is represented by the factor $I(f)$. The anelastic attenuation effect, to which we are interested, is described by the term $\exp(-\pi t^* f)$, where the t^* operator is

$$t^*_{i,j} = \int_{\text{ray}} \frac{ds}{v(s)Q(s)}. \tag{2}$$

The term ds is a raypath element, whereas $Q(s)$ and $v(s)$ represent the quality factor and the velocity along the ray, respectively. The relation between $Q(s)$ and t^* is linear as the raypath depends only on the known velocity structure. We assume here a frequency-independent Q.

Usually, the amplitude variations due to elastic properties of the medium are explained by a simple exponential form $|r|^{-\nu}$: r is the distance from the source and ν is the geometrical-spreading law exponent. This assumption is equivalent to consider the term $G(f, x)$ frequency independent. Therefore, let us consider a common-shot configuration and two receivers, having the same instrumental response curve, at different distances from the source. By assuming the factor $C(f)$ independent of frequency [*Kanamori*, 1967a; *Kanamori*, 1967b] and by taking the natural logarithm of the ratio of spectral amplitudes at two receivers (equation (1)), we deduce the expression

$$\ln\frac{A_2(f)}{A_1(f)} = \ln\frac{G(t_2)C_2}{G(t_1)C_1} - \pi\left(t_2^* - t_1^*\right)f \tag{3}$$

"with a linear slope c equals to $\pi\left(t_2^* - t_1^*\right)f$" [*Matheney and Nowack*, 1995]. The Δt^* is measured by linear fitting the spectral ratio in the least squares sense: the linear trend being a quality control of the fit. Δt^* value contains the information about the difference of wave attenuation along two different seismic rays arriving at two stations from the same source.

Appropriate synthetic tests suggest that, in our experimental configuration, the approximation of a frequency-independent geometrical-spreading term may provide inaccurate Δt^* measurements (see Text S1 and Figure S1 in the supporting information). Therefore, to obtain more reliable Δt^* measurements, a procedure proposed by *Sams and Goldberg* [1990] and *Xie* [2010] is tested and applied. It is based on the computation of a "reduced amplitude spectrum," from which the contributions of the fine velocity structure of the Earth on signal amplitudes, represented by the term $G(f, x)$, are removed through a "deconvolution procedure." The elastic Green's function in a heterogeneous medium may be approximately estimated by adopting a reference velocity and density structure, which are taken as 1-D structures.

For data analysis, first we compute displacement amplitude spectra of the real data by using a 0.248 s wide time window, containing the P wave onset, and a 5% cosine taper. Synthetic tests validated the choice of the time window, where a conservative criterion is considered: spurious converted arrivals should be avoided as they contaminate P wave first arrival spectrum (see Figure S2). Next, a three-point-wide averaging moving window is used to smooth the amplitude spectra to mitigate also the possible site effects on them. The same processing is applied to a presignal noise window having the same duration so that, for each seismogram, the signal-to-noise ratio (SNR) could be computed. All signals having an average SNR less than 5 are discarded.

Then, for each source-receiver couple of the SERAPIS experiment, the term $G(f, x)$ in a complete elastic medium is computed via an exact modeling code AXITRA for stratified media while neglecting the effect of the attenuation [*Coutant*, 1989]. Axitra implements the discrete wave-number *Bouchon's* [1979] integration in conjunction with reflectivity method [*Kennett*, 1983]. The elastic properties are represented by a depth-averaged P wave velocity model inferred from the 3-D velocity model of *Battaglia et al*. [2008] and by a density profile inferred from density values of rock samples reported in *Zamora et al*. [1994] and from gravity surveys [*Berrino et al*., 2008]. Next, each real displacement spectrum is deconvolved by the corresponding theoretical elastic Green's function obtaining the *reduced amplitude spectra*, where the influence of the propagation is mitigated.

Finally, spectral ratios of reduced amplitude spectra are computed in a common-source gather configuration. For each shot, to minimize the attenuation effect, we choose the closest receiver to the source as reference station that is the receiver with respect to which spectral ratio is computed. In order to take into account the noise influence in Δt^* measurements, spectral ratios are computed only for those frequencies for which both spectral amplitudes have a SNR greater than 5. In that way, less than 5% of amplitude values are discarded in the frequency range of 10–20 Hz, whereas more than 10% are discarded for frequencies greater than 30 Hz. Then, from 30 Hz on, the noise contribution starts to become significant with respect to signal amplitudes, leading to a too small number of selected amplitudes for proper estimation of Δt^*.

Before the fitting procedure, the retrieved spectral ratios are smoothed with a three-point-wide averaging moving window to obtain a more linear trend over a defined frequency range. Later, spectral ratios are fitted in the frequency range of 6–25 Hz (Figure 2a). The lower-frequency limit is chosen to discard spectral amplitudes affected by smoothing procedure. The higher-frequency limit is based on the previous consideration

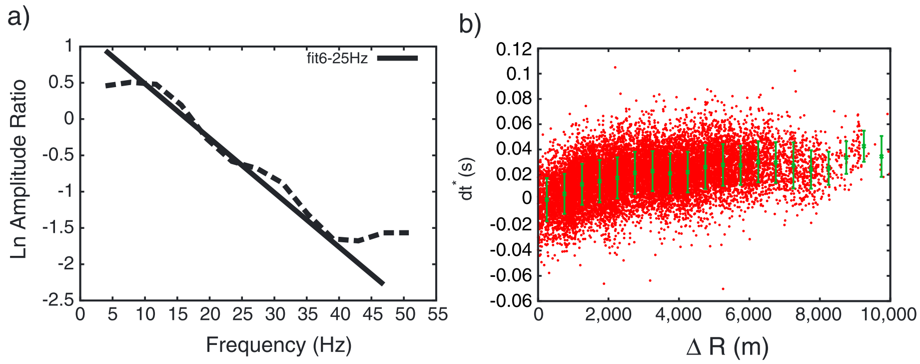

Figure 2. Spectral ratio fitting and retrieved Δt^* database. (a) Example of a computed spectral ratio (dashed line). The solid line is the spectral ratio best fit line, in the frequency range of 6–25 Hz. (b) Final Δt^* distribution consisting in 14,450 data computed by fitting spectral ratios in the frequency range of 6–25 Hz. The green points are the Δt^* mean values computed in ΔR ranges of 500 m. The green error bars are the data dispersion around the Δt^* mean value. The quantity ΔR, for each Δt^*, represents the difference between the distances between the source and the two receivers, respectively.

on SNR threshold. This time series procedure provides a preliminary Δt^* database, which is further analyzed through an additional selection:

1. All spectral ratios having a linear correlation coefficient $|R| > 0.95$ are selected.
2. The variance of residuals between the selected spectral ratios and their best fit lines is computed.
3. The average value of variance of residuals is computed.
4. Only spectral ratios (and their Δt^* estimates) having a variance of residuals value lower than the average one are selected.

This selection criterion provides a final Δt^* database of 14,450 measurements (Figure 2b).

2.2. Tomographic Method

Getting spatial distribution of Q_P factor from Δt^* measurements is performed by a tomographic approach based on an algorithm using an iterative, linearized, damped inversion technique [*Latorre et al.*, 2004]. A modified version of the attenuation tomography code by *Amoroso et al.* [2014] was modified for our purposes. A tomographic grid of regularly spaced nodes describes the subsurface. The inversion code solves a mixed determined system of equations [*Menke*, 1984] to minimize the misfit between observed and theoretical Δt^* values.

The geographical configuration of shots and receivers in Pozzuoli Bay allows us to study an area of 13×13 km^2. First, seismic rays are traced in a depth-averaged V_p model inferred from *Battaglia et al.* [2008] velocity model. The maximum depth of the tomographic grid is fixed to 1.5 km to reduce the number of underdetermined parameters in the inversion. Therefore, seismic rays deepening below 1.4 km are discarded, reducing the database to a total of 11,873 Δt^*. By comparing both resolution matrix (resolution diagonal element and spread function S_F [*Michelini and McEvilly*, 1991]) and derivative weight sum (DWS) [*Toomey and Foulger*, 1989] computed in a 1.5 km and 3 km deep tomographic grids, it emerges that resolutions in the first kilometer are comparable (Figures S3, S5, S6, and S7). DWS measures the ray density at inversion nodes. S_F is calculated by compressing each row of the resolution matrix into a parameter describing how peaked the resolution is for that node: the lower the S_F the more peaked is the resolution. Moreover, ad hoc checkerboard tests (Text S3 and Figure S4) show a very high recovery performance of the synthetic anomalies in the shallowest layers up to 1 km.

Optimal spacing of the inversion grid is obtained through several inversions by using different grid parameterizations: $1 \times 1 \times 0.5$ km^3, $0.5 \times 0.5 \times 0.5$ km^3, $0.5 \times 0.5 \times 0.25$ km^3, and $0.25 \times 0.25 \times 0.25$ km^3. As a starting model during these inversions, different homogeneous Q_P structures are used [*Martinez-Arevalo et al.*, 2005; *Chiarabba et al.*, 2009; *Bisrat et al.*, 2013]. Values of Q_P ranging from 30 to 150, with a step of 10, are tested [*Hansen et al.*, 2004; *Lin*, 2014]. The one producing the greatest reduction of Δt^* residuals at the first iteration is selected for further iterations: the initial uniform value Q_P is found to be 70 (Figure S8). The best discretization is chosen based on the corrected Akaike information criterion (AIC$_c$) [*Cavanaugh*, 1997], which is a statistical comparison [*Akaike*, 1974] between models characterized by a different number of parameters used. The minimum AIC_c value, representing the best compromise between reduction of data misfit and model simplicity, is obtained with the $1 \times 1 \times 0.5$ km^3 grid spacing. This is the parameterization adopted for the tomographic inversion. The computation and comparison of resolution matrix relative to parameterizations $1 \times 1 \times 0.5$ km^3 and $0.5 \times 0.5 \times 0.5$ km^3 confirm the goodness of our choice (Figures S5 and S6).

To ensure numerical stability and to control the model roughness a solution in the sense of damped least squares is searched [*Menke*, 1984]; the following function is minimized:

$$\phi(m) = (d - Gm)^T(d - Gm) + \varepsilon^2(m - m_0)^T(m - m_0) + Lm^T D^T Dm. \quad (4)$$

The term m_0 represents the vector of initial model parameters, whereas the term D represents the second derivative smoothing operator. In equation (4), two weighting, regularization, dimensionless factors ε^2 and L (damping and smoothing parameter, respectively) are present. The smoothing degree in the different directions is defined through parameters L_x, L_y, and L_z. The smoothing of the solution is achieved by constraining the Laplacian of the attenuation field to be zero [*Benz et al*., 1996]. To determine the best combination of regularization parameters in the inversion problem a recursive procedure fully described in the supporting information (Text S3 and Figure S9) is followed [*Rawlinson et al*., 2006]. Finally, $\varepsilon^2 = 0.7$, $L_x = L_y = 0.1$, and $L_z = 0.35$ are selected.

Furthermore, we explore the negligible effect of the choice of the initial attenuation model on the final result. Two hundred starting layered Q_P attenuation models are randomly generated within two extreme attenuation models [*Vanorio et al*., 2005]. For each initial model, an inversion is run. The final average attenuation image is computed as well as the normalized standard deviation (σ/Q_P) for each model parameter (Figure S10). We observe the average Q_P model showing the same features retrieved starting from a homogeneous $Q_P = 70$ model that is the chosen starting model (Figure 3). Only very small differences in the absolute quality factor values are found. Moreover, σ/Q_P values are, on average, less than 20% except for a very small number of grid nodes, mainly located in the poorly resolved areas of the tomographic grid.

3. Results

The inversion of Δt^* measurements is stopped at the fifth iteration as the model is not significantly modified afterward: it provides a Q_P model reducing the variance of Δt^* residuals to a value of 14% relative to a starting value of 2.7×10^{-4} s.

Figure 3a shows the plane view of the retrieved 3-D Q_P model, which describes a medium characterized by relatively low-Q_P, high-attenuation layers. On average, Q_P values less than 50 are widely present. The lowest retrieved values are $Q_P = 30$, in the shallowest part of the model. Several higher-Q_P anomalous bodies are recovered in the studied area, both at shallow and at greater depths. The maximum retrieved Q_P value is 230.

At 250 m depth, the continuous 3-D attenuation model shows two high-Q_P bodies (Q_P~200). A W-E structure is present in the central part of the Pozzuoli Bay, almost connecting Capo Miseno with Nisida Island. A subcircular anomalous high-Q_P body (maximum Q_P~200) is recovered south of Capo Miseno.

The $z = 500$ m plot shows four isolated, lower attenuation, small bodies ($Q_P \approx 150$). These are located (1) in the northeastern part of the Pozzuoli Bay, (2) in a region close to Capo Miseno, and (3) in the southern part of CF caldera. The low-attenuating bodies enclose an arc-like low-Q_P structure ($Q_P \approx 40$).

The 750 m depth map shows a continuous W-E structure having maximum Q_P values equal to 140, connecting north of Capo Miseno and Nisida Island. In the southern part of the bay lower Q_P bodies, with values around 100, are present. As in the previous depth slice, the described intermediate-Q_P bodies surround an arc-like attenuating structure from Capo Miseno to Nisida Bank.

At 1 km depth, a high-Q_P structure extends in the east direction toward Nisida Island. Moreover, in the southern part of the bay a continuous annular-like anomaly with Q_P values ranging from 90 to 130 is present. Finally, at 1.25 km and 1.4 km depth, isolated intermediate values, Q_P anomalies are found.

We also plot the Q_P variations in three W-E sections (A-A′, B-B′, and C-C′) crossing the tomographic model from north to south at $y = 5$ km, $y = 7.5$ km, and $y = 9$ km, respectively (Figure 3b). Section A-A′ mainly shows

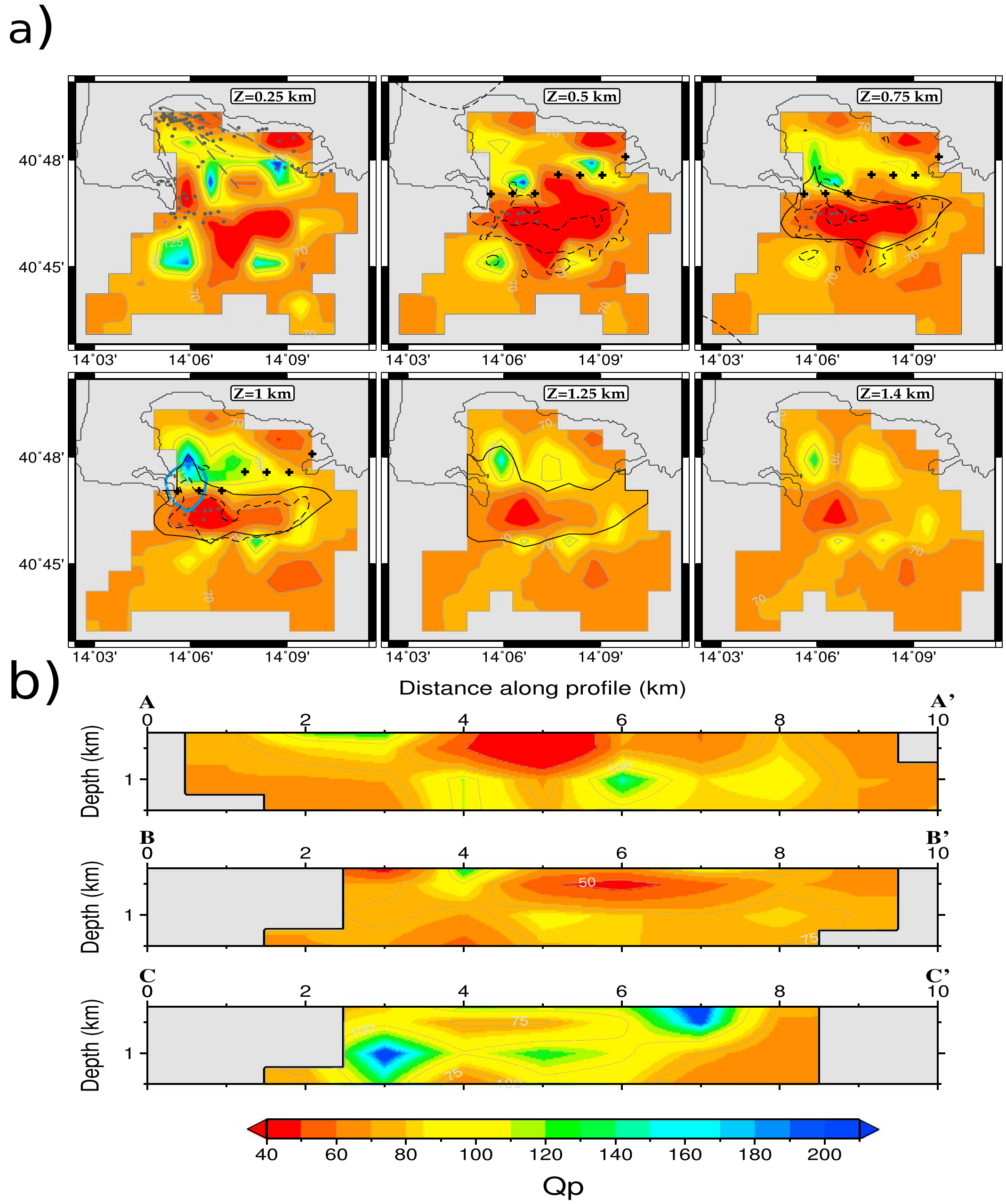

Figure 3. The 3-D Q_P image of the shallowest subsurface of CF caldera. (a) Plane view of the 3-D Q_P model at different depths. The gray regions represent the areas not covered by rays. The dark gray dots in the $z = 0.25$ km plot correspond to the fumaroles as reported in *De Bonitatibus et al.* [1970]. In the same plot, the gray dashed lines represent the traces of faults as reported in *Orsi et al.* [2004] and *Acocella* [2010]. In the $z = 0.5$ km, $z = 0.75$ km, and $z = 1$ km plots, the black crosses identify the high-scattering zones by *Tramelli et al.* [2006]. Dashed black lines: contour of high-V_p anomaly retrieved by *Dello Iacono et al.* [2009]. Solid black lines in plots $z = 0.75$ km, $z = 1$ km, and $z = 1.25$ km: high-V_p anomaly by *Battaglia et al.* [2008]. Solid blue contour in $z = 1$ km plot: low-V_p/V_s anomaly by *Chiarabba and Moretti* [2006]. (b) Section view of the 3-D Q_P model. The traces of the sections are reported in Figure 1.

a bowl-shape structure anomaly ($Q_P = 90$–140) enclosing a low-Q_P body ($Q_P = 40$) reaching a maximum depth of about 1 km. In section B-B′, Q_P range from 50 to 120 and the highest values are recovered at shallow depths, at 4 km distance. Profile C-C′ shows the highest-Q_P values with respect to other sections. A low-attenuation body ($Q_P = 200$), between 6 and 8 km in the horizontal direction, and between 250 m and 600–700 m depth, is imaged. At 1 km depth a subcircular structure, associated with an elongated one, is present.

The Q_P parameter uncertainty is estimated by mapping random deviates on data in the model parameter space [*Vasco and Johnson*, 1998]. Two hundred different databases are inverted by starting from a homogeneous $Q_P = 70$ attenuation model and by using the same parameterization and previously determined regularization parameters. Each database is obtained by adding to the measured Δt^* quantities a uniform random error in the range of the estimated data uncertainties. Then, the average attenuation model and the normalized standard deviation, σ/Q_P, were computed (Figure S11). The errors on parameters are lower than 5%, confirming that the Q_P absolute values retrieved by the tomographic inversion do not depend on data uncertainties. We assess the reliability of the tomographic image through resolution matrix and proper checkerboard tests that we already introduced in the previous paragraph and fully described in Text S2 and Figures S3a, S4a, S5a, and S6a. Resolution study confirms the accuracy of results, allowing to assert that the main features retrieved and interpreted by us are included in the most resolved area of the tomographic grid.

4. Discussion and Conclusions

The results of this study add important elements to understand the properties of the shallowest subsurface of Campi Flegrei caldera, down to 1–1.25 km depth. Indeed, to our best knowledge, no previous Q_P mappings are available in the same geographic area achieving a similar resolution. To gain insight into the volcanic structure of CF we compare our results with those provided by previous studies in the area: *P* and *S* wave tomographies [*Zollo et al*., 2003; *Chiarabba and Moretti*, 2006; *Battaglia et al*., 2008; *Dello Iacono et al*., 2009], gravimetric images [*Capuano et al*., 2013], scattering analyses [*Tramelli et al*., 2006], and seismic reflection profiles [*Pescatore et al*., 1984]. Moreover, we consider previous laboratory studies [*Ito et al*., 1979; *Winkler and Nur*, 1979] to confirm interpretations given to retrieved results.

First, in this study we recover an average *P* wave quality factor equal to 60–70: it is approximately the value of the starting attenuation model used for the 3-D tomographic inversion, although we showed that it does not affect the final solution. Previous attenuation studies of active volcanic and geothermal areas throughout the world [e.g., *Ward and Young*, 1980; *Sudo*, 1991; *Zucca et al*., 1994; *Shapiro et al*., 2000] retrieved similar Q_P values. Moreover, low-Q_P bodies (30–80) at 0.25 km depth and spatially correlated with low-V_p values are in agreement with those provided by *Clawson et al*. [1989] in Yellowstone National Park and by *De Gori et al*. [2005] at Mount Etna: they interpreted low-Q_P, low-V_p correlation as caldera filled by sediments and loose volcanic materials. *Johnston et al*. [1979] and *Amalokwu et al*. [2014], via ultrasonic laboratory measurements, retrieved similar Q_P values on sandstone samples. On these grounds, we interpret the low-Q_P values retrieved in the shallowest subsurface of the offshore region of CF caldera as water-saturated volcanic and marine sediments [*Dello Iacono et al*., 2009]. After all, *Sacchi et al*. [2014] retrieved in core samples in Pozzuoli Bay mud, sandy silt, and volcaniclast-composed sediments.

A prominent feature revealed by our results and visible from 0.5 km to 1.25 km depths is an arc-like, high-attenuating structure extending from Capo Miseno to the south of Nisida Island (Q_P values around 40–50). This structure matches well the high-V_p anomaly retrieved first by *Zollo et al*. [2003] and furtherly confirmed by *Battaglia et al*. [2008] and *Dello Iacono et al*. [2009] and highlighted by solid and dashed black contour in Figure 3a, respectively. *Capuano et al*. [2013] found a positive gravity anomaly in the same area. These anomalies are interpreted as the buried rim of the CF caldera, composed of an intercalation of consolidated tuffs and trachytic lavas. Moreover, ultrasound surveys revealed fumaroles close to Capo Miseno [*De Bonitatibus et al*., 1970]. In the same range of depths, *Tramelli et al*. [2006] imaged a high-scattering zone partially superimposing to the high-V_p anomaly. They found also a correspondence between high-scattering zones, fumaroles, and low-Q_P regions in the area of Solfatara crater, interpreting it as densely fractured, porous, and fluid-filled rocks. *De Gori et al*. [2005] explained the correlation of low-Q_P and high-V_p at Mount Etna as fractured hot fluid-saturated rocks. For these reasons, we suggest that the described feature in this attenuation model is due to a densely fractured rock volume, partially saturated in fluids [*Winkler and Nur*, 1979]; the latter are probably linked to the fumaroles located in correspondence of the buried rim of CF caldera.

In correspondence of the southern shallower high-Q_P bodies ($z = 0.25$–0.5 km), there are submerged monogenic volcanic edifices (Miseno Bank and Pentapalummo Bank) belonging to the precalderic activity of CF [*Barberi et al*., 1991]. The location of this belt of submarine volcanoes well matches high magnetic anomalies [*Napoleone et al*., 1984; *Siniscalchi et al*., 2002; *Aiello et al*., 2005]. Seismic profiles acquired by

Pescatore et al. [1984] in Pozzuoli Bay unveiled an acoustically dull body in the zone of Pentapalummo Bank, whose margins are composed of volcanic deposits overlaying a massive volcanic body. *Napoleone et al*. [1984], furthermore, interpreted the high magnetic anomalies in the zone of submarine volcanic belts as linked to the presence of a buried igneous body. Therefore, a possible interpretation of these shallow high-Q_P bodies is the combination of consolidated volcanic materials and magma-cooled material.

Finally, in the inner part of CF caldera, a heterogeneous distribution of high-Q_P and low-Q_P bodies is correlated at each depth with low-V_p values. In the same range of depths, *Dello Iacono et al*. [2009] found an average high V_p/V_s ratio (3.7 ± 0.9), interpreting it as the signature of fully saturated sediments. Moreover, in the inner caldera, faults and fumaroles partially overlapping to attenuation anomalies were recognized by *De Bonitatibus et al*. [1970], *Orsi et al*. [2004], and *Acocella* [2010]. We therefore suggest that the heterogeneity in the anelastic features may reflect the different saturation conditions of volcanic sediments, which were only partially mapped in this geographic area by *Vanorio et al*. [2005], *Chiarabba and Moretti* [2006], and *Battaglia et al*. [2008]. In particular, following *Winker and Nur* [1979], high-Q_P anomalies may be interpreted as fully saturated sediments, whereas low-Q_P bodies may describe partially saturated sediments. The anticorrelation of high-Q_P bodies with low-V_p values in a zone very rich in fumaroles and faults may also be explained as the effect of fluids standing in vapor state, as justified by *Ito et al*. [1979]. This interpretation could be particularly valid for the high-Q_P body found at 1 km depth close to Capo Miseno and also visible in the section C-C′ at a distance of 3 km along the profile. Actually, this attenuation anomaly partially overlaps a low V_p/V_s ratio retrieved by *Chiarabba and Moretti* [2006] at the same depth and highlighted by blue solid contour. This low V_p/V_s ratio is mainly representative of gas saturation instead of presence of fluids. The possible role of faults recognized in this area is that of preferential ways of degassing.

Our work, through a three-dimensional Q_P model, outlines the rheological properties of the buried rim of CF caldera previously detected by seismic velocity tomography. The anelastic model allows us to describe the rim as a fluid-filled, densely fractured rock volume. Moreover, the heterogeneities in the distribution of Q_P anomalies in the inner caldera are interpreted as the possible effect of the different conditions of saturation of the sediments.

Acknowledgments
Waveform data may be requested to Aldo Zollo, the supervisor of the seismological laboratory of Department of Physics "E. Pancini" (University of Naples, Federico II). This work was funded by University of Naples Federico II and the University of Bologna Alma Mater Studiorum. Moreover, AMRA s.c. ar.l. partially funded this work in the framework of MedSuv Project, which received funding from the European Union Seventh Programme for research, technological development, and demonstration, under grant agreement 308665. Spectral analysis and some of the figures were made by using GNUPLOT (http://www.gnuplot.info/), Seismic Analysis Code (which can be requested from the Incorporated Research Institutions for Seismology; http://www.iris.edu) and Generic Mapping Tools (www.soest.hawaii.edu/gmt) [*Wessel and Smith*, 1991]. Elastic Green's functions are computed using the AXITRA code of *Coutant* [1989]. Special thanks to Anna Tramelli, Milena Moretti, Dario Dello Iacono, and Maurizio Vassallo for providing us their scattering and velocity models used for better constraining the interpretation given to our results. Special thanks, also, to all members of the seismological laboratory of the Department of Physics E. Pancini (University of Naples, Federico II) for their fruitful discussions and comments. We acknowledge two anonymous reviewers for their careful revision of our manuscript.

References

Acocella, V. (2010), Evaluating fracture patterns within a resurgent caldera: Campi Flegrei, Italy, *Bull. Volcanol.*, *72*, 623–638, doi:10.1007/s00445-010-0347-x.

Aiello, G., A. Angelino, B. D'Argenio, E. Marsella, N. Pelosi, S. Ruggieri, and A. Siniscalchi (2005), Buried volcanic structures in the Gulf of Naples (Southern Tyrrhenian Sea, Italy) resulting from high resolution magnetic survey and seismic profiling, *Ann. Geophys.*, *48*(6), 1–15, doi:10.3301/ag-3241.

Akaike, H. (1974), A new look at the statistical model identification, *IEEE Trans. Autom. Control*, *6*, 716–723.

Amalokwu, K., A. I. Best, J. Sothcott, M. Chapman, T. Minshull, and X. Li (2014), Water saturation effects on elastic wave attenuation in porous rocks with aligned fractures, *Geophys. J. Int.*, *197*(2), 943–947, doi:10.1093/gji/ggu076.

Amoroso, O., G. Russo, A. Orefice, J. Virieux, and A. Zollo (2014), 3D seismic imaging of the Irpinia fault system (southern Italy) from multi-scale velocity and attenuation tomography paper presented at the 2nd European Conference on Earthquake Engineering and Seismology, Istanbul, Turkey.

Barberi, F., E. Cassano, P. La Torre, and A. Sbrana (1991), Structural evolution of Phlegrean Fields in light of volcanological and geophysical data, *J. Volcanol. Geotherm. Res.*, *48*(1), 33–49, doi:10.1016/0377-0273(91)90031-T.

Battaglia, J., A. Zollo, J. Virieux, and D. Dello Iacono (2008), Merging active and passive data sets in travel time tomography: The case study of Campi Flegrei caldera (southern Italy), *Geophys. Prospect.*, *56*, 555–573, doi:10.1111/j.1365-2478.2007.00687.x.

Benz, H. M., B. A. Chouet, P. B. Dawson, J. C. Lahar, R. A. Page, and J. Hole (1996), Three dimensional *P* and *S* wave velocity structure of Redoubt Volcano, Alaska, *J. Geophys. Res.*, *101*(B4), 8111–8128, doi:10.1029/95JB03046.

Berrino, G., G. Corrado, and U. Riccardi (2008), Sea gravity data in the gulf of Naples: A contribution to delineating the structural pattern of the Phlegrean volcanic district, *J. Volcanol. Geotherm. Res.*, *175*(3), 241–252, doi:10.1016/j.jvolgeores.2008.03.007.

Bisrat, S. T., H. R. DeShon, J. Pesicek, and C. Thurber (2013), High-resolution 3-D *P* wave attenuation structure of the New Madrid Seismic Zone using local earthquake tomography, *J. Geophys. Res. Solid Earth*, *119*, 409–424, doi:10.1002/2013JB010555.

Bouchon, M. (1979), Discrete wave-number representation of elastic wave field in three-space dimensions, *J. Geophys. Res.*, *84*, 3609–3614, doi:10.1029/JB084iB07p03609.

Brenguier, F., O. Coutant, H. Baudon, F. Dorè, and M. Dietrich (2006), High resolution seismic tomography of a Strombolian volcanic cone, *Geophys. Res. Lett.*, *33*, L16314, doi:10.1029/2006GL026902.

Capuano, P., and U. Achauer (2003), Gravity field modeling in the Vesuvius and Campanian area, in *The TomoVes Seismic Project: Looking Inside Mt. Vesuvius [CD-ROM]*, edited by A. Zollo et al., Coop. Univ. Editrice Napoletana, Naples, Italy.

Capuano, P., et al. (2006), Campi Flegrei active seismic experiments waveforms compilation, in *Geophysical Exploration of the Campi Flegrei (Southern Italy) Caldera's Interior: Data, Methods and Results*, edited by A. Zollo et al., pp. 79–87, GNV, Naples, Italy.

Capuano, P., G. Russo, L. Civetta, G. Orsi, M. D'Antonio, and R. Moretti (2013), The active portion of the Campi Flegrei caldera structure imaged by 3-D inversion of gravity data, *Geochem. Geophys. Geosyst.*, *14*, 4681–4697, doi:10.1002/ggge.20276.

Cavanaugh, J. E. (1997), Unifying the derivations for the Akaike and corrected Akaike information criteria, *Stat. Probab. Lett.*, *33*(2), 201–208.

Chiarabba, C., and M. Moretti (2006), An insight into the unrest phenomena at the Campi Flegrei caldera from V_p and V_p/V_s tomography, *Terra Nova*, *18*, 373–379, doi:10.1111/j.1365-3121.2006.00701.x.

Chiarabba, C., D. Piccinini, and P. De Gori (2009), Velocity and attenuation tomography of the Umbria-Marche 1997 fault system: Evidence of a fluid-governed seismic sequence, *Tectonophysics*, *476*, 73–84, doi:10.1016/j.tecto.2009.04.004.

Clawson, S. R., R. B. Smith, and H. M. Benz (1989), P Wave attenuation of the Yellowstone caldera from three-dimensional inversion of spectral decay using explosion source seismic data, *J. Geophys. Res.*, *94*(B6), 7205–7222, doi:10.1029/JB094iB06p07205.

Coutant, O. (1989), Program of numerical simulation AXITRA Tech. Rept., LGIT, Grenoble, France.

De Bonitatibus, A., G. Latmiral, G. Latmiral, L. Mirabile, A. Palumbo, E. Sarpi, and A. Scalera (1970), Rilievi sismici per riflessione: Strutturali, ecografici (fumarole) e batimetrici, nel golfo di Pozzuoli, *Boll. Soc. Nat. Napoli*, *79*, 97–113.

De Gori, P., C. Chiarabba, and D. Patanè (2005), Q_P structure of Mount Etna: Constraints for the physics of the plumbing system, *J. Geophys. Res.*, *110*, B05303, doi:10.1029/2003JB002875.

de Lorenzo, S., A. Zollo, and F. Mongelli (2001), Source parameters and three-dimensional attenuation structure from the inversion of microearthquake pulse width data: Q_P imaging and inferences on the thermal state of Campi Flegrei caldera (southern Italy), *J. Geophys. Res.*, *106*(B8), 16,265–16,286, doi:10.1029/2000JB900462.

De Siena, L., E. Del Pezzo, and F. Bianco (2010), Seismic attenuation imaging of Campi Flegrei: Evidence of gas reservoirs, hydrothermal basins, and feeding systems, *J. Geophys. Res.*, *115*, B09312, doi:10.1029/2009JB006938.

De Siena, L., C. Thomas, G. P. Waite, S. C. Moran, and S. Klemme (2014), Attenuation and scattering tomography of the deep plumbing system of Mount St. Helens, *J. Geophys. Res. Solid Earth*, *119*, 8223–8228, doi:10.1002/2014JB011372.

De Vivo, B., G. Rolandi, P. B. Gans, A. Calvert, W. A. Bohrson, F. J. Spera, and H. E. Belkin (2001), New constraints on the pyroclastic eruptive history of the Campanian volcanic plain (Italy), *Mineral. Petrol.*, *73*, 47–65.

Deino, A. L., G. Orsi, S. de Vita, and M. Piochi (2004), The age of the Neapolitan Yellow Tuff caldera-forming eruption (Campi Flegrei caldera, Italy) assessed by ^{40}Ar/^{39}Ar dating method, *J. Volcanol. Geotherm. Res.*, *133*, 157–170, doi:10.1016/S0377-0273(03)00396-2.

Dello Iacono, D., A. Zollo, M. Vassallo, T. Vanorio, and S. Judenherc (2009), Seismic images and rock properties of the very shallow structure of Campi Flegrei caldera (southern Italy), *Bull. Volcanol.*, *71*, 275–284, doi:10.1007/s00445-008-0222-1.

Hansen, S., C. H. Thurber, M. Mandernach, F. Haslinger, and C. Doran (2004), Seismic velocity and attenuation structure of the east rift zone and south Flank of Kilauea Volcano, Hawaii, *Bull. Seismol. Soc. Am.*, *94*(4), 1430–1440, doi:10.1785/012003154.

Ito, H., J. DeVilbiss, and A. Nur (1979), Compressional and shear waves in saturated rock during water-steam transition, *J. Geophys. Res.*, *84*, 4731–4735, doi:10.1029/JB084iB09p04731.

Johnston, D. H., M. N. Toksoz, and A. Timu (1979), Attenuation of seismic waves in dry and saturated rocks: II. Mechanisms, *Geophysics*, *44*(4), 691–711, doi:10.1190/1.1440970.

Judenherc, S., and A. Zollo (2004), The Bay of Naples (southern Italy): Constraints on the volcanic structure inferred from a dense seismic survey, *J. Geophys. Res.*, *109*, B10312, doi:10.1029/2003JB002876.

Kanamori, H. (1967a), Spectrum of *P* and *PcP* in relation to the mantle-core boundary and attenuation in the mantle, *J. Geophys. Res.*, *72*(2), 559–571, doi:10.1029/JZ072i002p00559.

Kanamori, H. (1967b), Spectrum of short-period core phases in relation to the attenuation in the mantle, *J. Geophys. Res.*, *72*(8), 2182–2186, doi:10.1029/JZ072i008p02181.

Kennet, B. L. N. (1983), *Seismic Wave Propagation in Stratified Media*, Cambridge Univ. Press, Cambridge.

Latorre, D., J. Virieux, T. Monfret, V. Monteiller, T. Vanorio, J.-L. Got, and H. Lyon-Caen (2004), A new seismic tomography of Aigion area (Gulf of Corinth, Greece) from the 1991 data set, *Geophys. J. Int.*, *159*(3), 1013–1031, doi:10.1111/j.1365-246X.2004.02412.x.

Lin, G. (2014), Three-dimensional compressional wave attenuation tomography for the crust and uppermost mantle of northern and central California, *J. Geophys. Res. Solid Earth*, *119*, 3462–3477, doi:10.1002/2013JB010621.

Martinez-Arevalo, C., D. Patanè, A. Rietbrock, and J. M. Ibanez (2005), The intrusive process leading to the Mt. Etna 2001 flank eruption: Constraints from 3-D attenuation tomography, *Geophys. Res. Lett.*, *32*, L21309, doi:10.1029/2005GL023736.

Matheney, P. M., and R. Nowack (1995), Seismic attenuation values obtained from instantaneous-frequency matching and spectral ratios, *Geophys. J. Int.*, *123*, 1–15, doi:10.1111/j.1365-246X.1995.tb06658.x.

Menke, W. (1984), *Geophysical Data Analysis: Discrete Inverse Theory*, Academic Press, Inc, San Diego, Calif.

Michelini, A., and T. A. McEvilly (1991), Seismological studies at Parkfield. I. Simultaneous inversion for velocity structure and hypocenters using cubic B-splines parameterization, *Bull. Seismol. Soc. Am.*, *81*(2), 524–552.

Napoleone, G., M. Ripepe, and E. Ruggiero (1984), Contributi allo studio del golfo di Pozzuoli: Strutture episuperficiali dedotte dal rilievo magnetico, *Mem. Soc. Geol. Ital.*, *27*, 205–211.

Orsi, G., S. M. Petrazzuoli, and K. Wholetz (1999), Mechanical and thermo-fluid behaviour during unrest at the Campi Flegrei caldera (Italy), *J. Volcanol. Geotherm. Res.*, *91*, 453–470.

Orsi, G., M. A. Di Vito, and R. Isaia (2004), Volcanic hazard assessment at the restless Campi Flegrei caldera, *Bull. Volcanol.*, *66*, 514–530, doi:10.1007/s00445-003-0336-4.

Pescatore, T., G. Diplomatico, M. R. Senatore, M. Tramutoli, and L. Mirabile (1984), Contributi allo studio del golfo di Pozzuoli: Aspetti stratigrafici e strutturali, *Mem. Soc. Geol. Ital.*, *27*, 133–149.

Prudencio, J., J. M. Ibáñez, A. García-Yeguas, E. Del Pezzo, and A. Posadas (2013), Spatial distribution of intrinsic and scattering seismic attenuation in active volcanic islands: II. Deception island images, *Geophy. J. Int.*, *195*(3), 1957–1969, doi:10.1093/gji/ggt360.

Prudencio, J., E. Del Pezzo, J. M. Ibáñez, E. Giampiccolo, and D. Patané (2015a), Two-dimensional seismic attenuation images of Stromboli Island using active data, *Geophys. Res. Lett.*, *42*, 1–8, doi:10.1002/2015GL063293.

Prudencio, J., L. De Siena, J. M. Ibáñez, E. Del Pezzo, A. García-Yeguas, and A. Díaz-Moreno (2015b), The 3D attenuation structure of Deception Island (Antarctica), *Surv. Geophys.*, *36*(3), 371–390, doi:10.1007/s10712-015-9322-6.

Prudencio, J., J. M. Ibáñez, E. Del Pezzo, J. Martí, A. García-Yeguas, and L. De Siena (2015c), 3D attenuation tomography of the volcanic island of Tenerife (Canary Islands, Spain), *Surv. Geophys.*, *36*(5), 693–716, doi:10.1007/s10712-015-9333-3.

Rawlinson, N., A. M. Reading, and B. L. N. Kennet (2006), Lithospheric structure of Tasmania from a novel form of teleseismic tomography, *J. Geophys. Res.*, *111*, B02301, doi:10.1029/2005JB/2005JB003803.

Rowlands, D. P., R. S. White, and A. J. Haines (2005), Seismic tomography of the Tongariro Volcanic Centre, New Zealand, *Geophys. J. Int.*, *163*, 1180–1194, doi:10.1111/j.1365-246X.2005.02716.x.

Sacchi, M., M. Pepe, M. Corradino, D. D. Insinga, F. Molisso, and C. Lubritto (2014), The Neapolitan Yellow Tuff caldera offshore the Campi Flegrei: Stratal architecture and kinematic reconstruction during the last 15 ky, *Mar. Geol.*, *354*, 15–33, doi:10.1016/j.margeo.2014.04.012.

Sams, M., and D. Goldberg (1990), The validity of *Q* estimates from borehole data using spectral ratios, *Geophysics*, *55*(1), 97–101, doi:10.1190/1.1442776.

Sanders, C. O., S. C. Ponko, L. D. Nixon, and E. A. Schwartz (1995), Seismological evidence for magmatic and hydrothermal structure in Long Valley caldera from local earthquake attenuation and velocity tomography, *J. Geophys. Res.*, *100*(B5), 8311–8326, doi:10.1029/95JB00152.
Shapiro, N. M., S. K. Singh, A. Iglesias-Mendoza, V. M. Cruz-Atienza, and J. F. Pacheco (2000), Evidence of low *Q* below Popocatépetl Volcano, and its implication to seismic hazard in Mexico City, *Geophys. Res. Lett.*, *27*(17), 2753–2756, doi:10.1029/1999GL011232.
Sherburn, S., R. S. White, and M. Chadwick (2006), Three-dimensional tomographic imaging of the Taranaki volcanoes, New Zealand, *Geophys. J. Int.*, *166*, 957–969, doi:10.1111/j.1365-246X.2006.03040.x.
Siniscalchi, A., A. Angelino, S. Ruggieri, G. Aiello, E. Marsella, and M. Sacchi (2002), High resolution magnetic anomaly map of the Bay of Naples (Southern Tyrrenian Sea, Italy), *Boll. Geofis. Teor. Appl.*, *42*(1/2), 99–103.
Sudo, Y. (1991), An attenuating structure beneath the Aso Caldera determined from the propagation of seismic waves, *Bull. Volcanol.*, *53*, 99–111.
Teng, T. (1968), Attenuation of body waves and the *Q* structure of the mantle, *J. Geophys. Res.*, *73*(6), 2195–2208, doi:10.1029/JB073i006p02195.
Toomey, D. R., and G. R. Foulger (1989), Tomographic inversion of local earthquake data from the Hengill-Grensdalur Central Volcano Complex, Iceland, *J. Geophys. Res.*, *94*(B12), 17,497–17,510, doi:10.1029/JB094iB12p17497.
Tramelli, A., E. Del Pezzo, F. Bianco, and E. Boschi (2006), 3D scattering image of the Campi Flegrei caldera (southern Italy). New hints on the position of the old caldera rim, *Phys. Earth Planet. Inter.*, *155*, 269–280, doi:10.1016/j.pepi.2005.12.009.
Vanorio, T., J. Virieux, P. Capuano, and G. Russo (2005), Three-dimensional seismic tomography from *P* wave and *S* wave microearthquake travel times and rock physics characterization of the Campi Flegrei caldera, *J. Geophys. Res.*, *110*, B03201, doi:10.1029/2004JB003102.
Vasco, D. W., and L. R. Johnson (1998), Whole Earth structure estimated from seismic arrival times, *J. Geophys. Res.*, *103*, 2633–2672, doi:10.1029/97JB02623.
Ward, R. W., and C.-Y. Young (1980), Mapping seismic attenuation within geothermal systems using teleseisms with application to the Geysers-Clear Lake region, *J. Geophys. Res.*, *85*, 5227–5236, doi:10.1029/JB085iB10p05227.
Wessel, P., and W. H. F. Smith (1991), Free software helps map and display data, *Eos Trans. AGU*, *72*, 445–446, doi:10.1029/90EO00319.
Winkler, K. W., and A. Nur (1979), Pore fluids and seismic attenuation in rocks, *Geophys. Res. Lett.*, *6*(1), 1–4, doi:10.1029/GL006i001p00001.
Xie, J. (2010), Can we improve estimates of seismological *Q* using a new geometrical spreading model? *Pure Appl. Geophys.*, *167*, 1147–1162, doi:10.1007/s00024-010-0188-8.
Zamora, M., G. Sartoris, and W. Chelini (1994), Laboratory measurements of ultrasonic wave velocities in rocks from the Campi Flegrei volcanic system and their relation to other field data, *J. Geophys. Res.*, *99*(B7), 553–561, doi:10.1029/94JB00121.
Zollo, A., et al. (2003), Evidence for the buried rim of Campi Flegrei caldera from 3-D active seismic imaging, *Geophys. Res. Lett.*, *30*(19), 2002, doi:10.1029/2003GL018173.
Zucca, J. J., L. J. Hutchings, and P. W. Kasameyer (1994), Seismic velocity and attenuation structure of the Geysers geothermal field, California, *Geothermics*, *23*(2), 111–126, doi:10.1016/0375-6505(94)90033-7.